An Experiment-Based Numerical Treatment of Spin Wave Modes in Periodically Porous Materials

Daniel Van Opdenbosch,* Golda Hukic-Markosian, Steven Ott, Claas Abert, and Michael H. Bartl*

To determine a general correlation between structure and dynamic magnetic properties of porous materials, the frequencies of magnetic spin waves are studied by Brillouin light scattering from nickel inverse opals and backed up by micromagnetic simulations. Within the observed unit cell size regime between 400 and 800 nm, discrete thickness standing modes are found to change with unit cell size. By applying pair correlation functions of the inverse opal solid phase normal to the applied field to an equation for perpendicular standing modes, the directional and unit cell size-dependent spectral intensities above the surface mode region can be traced. Thus, an accessible general approach for the prediction of standing spin waves in porous materials is obtained.

1. Introduction

The effect of material superstructure on the dynamic magnetic properties is a long-standing matter of interest in the field of magnetism.[1–5] This issue has received renewed attention with the emergence of magnonic crystals, which are periodically organized magnetic materials.[6–10] These have the potential to control spin wave propagation and densities of states of magnons, and thus provide entirely new, spin-based ways to transfer and process information without moving charges. Significant progress has been made in the fabrication and characterization of magnonic crystals with 1D[10–13] and 2D periodicity in form of dot[2,14–16] or antidot lattices,[8,17,18] or bicomponent composites.[19–22] Recently, Beginin et al. realized spin wave guidance in 3D magnonic crystals in the shape of layered meanders.[23]

Diverse routes to prepare 3D-structured magnonic crystals have been assessed.[24–27] However, research on the directional properties of 3D magnonic structures has been limited mainly to theoretical studies.[3,28,29] Krawczyk and Puszkarski developed a plane-wave theory for 3D magnonic crystals.[3] In addition, ab initio calculations were performed for 3D magnetic materials with spatial disorder.[28] However, to the best of our knowledge, there is no simple, numerically derived approach to determine the correlation between the 3D order of complexly structured magnetic materials and the characteristic magnetic spin wave modes resulting from spatial magnon confinement.

However, there is a need: Kostylev et al. reported, for 3D magnonic crystals in the shape of nickel inverse opals, ferromagnetic resonance spectra of differential absorption, which exhibit a complex fine structure with changing applied field.[30] In their own words, their "investigation revealed a broad band of frequencies and fields in which resonant absorption takes place. For the out-of-plane direction of magnetization, a number of partially resolved modes are observed."[30] These were accounted for by a model of "effective cylinders."

Having prepared similar materials in an earlier work,[27] we were intrigued by the prospect of a mode explanation, directly based on the inverse opal structure. Further motivation was provided by the outlook that such an approach could be adapted to any magnetic superstructure.

While micromagnetic simulations are a powerful tool to assess the spin wave mode spectra for magnetic materials, they require extensive preparation, powerful computing systems (typically numerous graphics processors running in parallel) and days to complete and evaluate. Finding analytical expressions for spin wave modes, on the other hand, is feasible for simple geometries such as spheroids,[31] spheres,[32] or slabs[4]; however, this method becomes impractical for structures with higher complexity. To illustrate, the tabulated resulting expressions for the

Dr. D. Van Opdenbosch
Chair of Biogenic Polymers
Technical University of Munich
Schulgasse 16, Straubing D-94315, Germany
E-mail: daniel@van-opdenbosch@tum.de

Dr. G. Hukic-Markosian, S. Ott, Prof. M. H. Bartl[+]
Department of Chemistry
University of Utah
315 S 1400 E, Salt Lake City, UT 84112, USA
E-mail: michael.bartl@utah.edu

Dr. C. Abert
Physics of Functional Materials
University of Vienna
Währinger Straße 17, Vienna A-1090, Austria

The ORCID identification number(s) for the author(s) of this article can be found under https://doi.org/10.1002/pssb.201900296.

[+]Present address: Center for Energy Efficient Electronics Science, University of California, Berkeley, 550 SDH Berkeley, CA94720-1770, USA

resonant modes of spheres span several pages.[32] Therefore, it is not suitable for the assessment of spin wave mode spectra expected from 3D magnetic superlattices. In this article, we present a simple, but widely adaptable, method for correlating 3D material structuring to resulting standing spin wave modes, using the example of an "anti-sphere" lattice in the form of an inverse opal magnetic material with face-centered cubic (FCC) symmetry.

The method consists of passing pair correlation functions through the inverse opals along all vectors normal to the applied magnetic field to the equation for thickness standing spin wave modes for several mode orders. The resulting predictions were based on initial observations from Brillouin light scattering (BLS) spectra recorded from nickel inverse opal samples, fabricated by colloidal self-assembly and electrodeposition. Due to ambiguities in the measured BLS spectra, dynamic micromagnetic simulations were performed to confirm predictions.

2. Experimental Section

2.1. Antisphere Lattice Model Structure

For the model structure of the 3D antisphere lattice, a nickel-based inverse opal material was chosen; its Brillouin zone vectors are shown in **Figure 1**a. The saturation magnetization M_s of 5×10^5 Am^{-1} for nickel was used for all simulations.[33] Sample axes were designated according to the right-hand rule. For comparison with results from BLS measurements on real samples (see Figure 1b), the experimental conditions were mirrored in the method of rapid prediction and the micromagnetic simulations of spin wave modes: the probing direction $\mathbf{k}$, the probing electrical field vector $\mathbf{E}_i$, and the externally applied field $\mathbf{H}_0$ remained fixed and perpendicular to one another. Generally, unscaled wavevector directions were denoted with $\mathbf{k}$ and their lengths with k. In predictions and simulations, as well as in the BLS measurements, samples were rotated from the crystallographic direction $(1|1|1)$ around the two axes $\mathbf{E}_i$ and $\mathbf{H}_0$, as shown in Figure 1b,c and listed in **Table 1**.

**Table 1.** Rotation-dependent probing directions **k** and applied magnetic field directions $\mathbf{H}_0$ expressed as the approximate Miller indices $(h|k|l)$ of the FCC inverse opals.

Rotation axis	Rotation angle [°]	k	$\mathbf{H}_0$
$\mathbf{E}_i$	60 ± 2	$(\bar{1}|3|1)$	$(12|2|7)$
$\mathbf{E}_i$	40 ± 2	$(0|2|1)$	$(5|\bar{1}|2)$
$\mathbf{E}_i$	20 ± 2	$(3|8|6)$	$(4|\bar{2}|1)$
—	0 ± 2	$(1|1|1)$	$(1|\bar{1}|0)$
$\mathbf{H}_0$	20 ± 2	$(5|5|2)$	$(1|\bar{1}|0)$
$\mathbf{H}_0$	40 ± 2	$(17|17|\bar{2})$	$(1|\bar{1}|0)$
$\mathbf{H}_0$	60 ± 2	$(3|3|\bar{2})$	$(1|\bar{1}|0)$

2.2. Nickel Inverse Opal Fabrication and Characterization

Nickel-based inverse opal samples were fabricated by electrochemical infiltration of nickel into FCC template structures of close-packed polymer spheres.[24,27,34,35] Details of the fabrication process are based on an earlier work[27] and are given in Supporting Information S1. In short, opal templates were assembled by vertical deposition from polystyrene spheres with diameters of 250, 390, 420, and 500 nm. Electrodeposition was used to backfill the opal voids with nickel metal. After removal of the templates by chemical dissolution of the polystyrene spheres, nickel inverse opal samples were obtained. Nonporous reference film samples were prepared by deposition without opal templates. For the purpose of this work, all samples were quasi-infinite planes. The reference film and the opals were 300 nm and 3 µm in thickness, respectively. The filling factors f of the different nickel inverse opal samples were determined from the final air sphere void radii r and the unit cell side lengths a, via Equation (1).

$$f = 1 - r^3 \frac{16\pi}{3a^3} \tag{1}$$
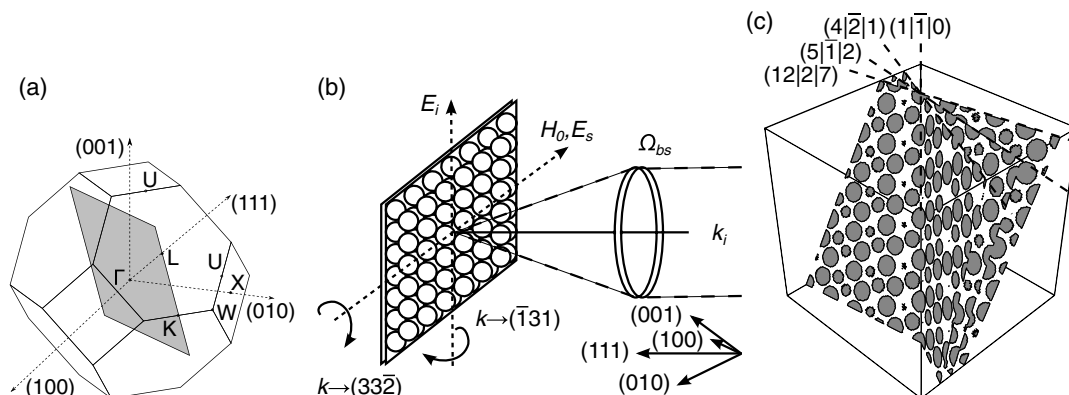
Figure 1. a) Sketch of the Brillouin zone of an FCC unit cell with the plane perpendicular to the $(1|\bar{1}|0)$ opal axis marked gray. b) Scheme of the BLS setup in backscattering geometry, indicating the sample rotation in the otherwise fixed setup. c) Slices through a super-cell measuring 6^3 FCC unit cells, normal to $\mathbf{H}_0$ with changing rotation around $\mathbf{E}_i$, solid material in white, with opal directions $(1|1|1)$ perpendicular, and $(1|\bar{1}|0)$ parallel to the drawing plane.

2.3. Brillouin Light Scattering

BLS measurements were carried out with a reference-stabilized triple-pass tandem Fabry–Pérot interferometer (TFP-1, JRS, Mettmannstetten, Switzerland). Magnetic fields were produced by a direct current electrically induced magnet (5403, GMW, San Carlos, CA, USA). The 532 nm line of a single-mode, diode-pumped, solid-state laser (CrystaLaser, Reno, NV, USA) operated at 100 mW continuous wave output power, and with electrical field vector direction $\mathbf{E}_i$, was further monochromatized by a temperature-stabilized fused-silica etalon (TCF-1, JRS, Mettmannstetten, Switzerland). Generally, $k_i = 2\pi/\lambda$ is used for the wavevector of the incoming laser beam. In our BLS experiments, performed in backscattering geometry as shown in Figure 1b, the direction $\mathbf{k} = \mathbf{k}_i$ is probed. The samples were mounted on a two-axes goniometer, which allowed tilting by angles up to 60°.

The focusing and collecting lens of diameter 50 mm had a focal length of 75 mm. Reflected light was collected and passed through a polarizer, allowing passage of the electrical field vector $\mathbf{E}_s \perp \mathbf{E}_i$, to suppress light inelastically scattered by interaction with phonons. It entered the interferometer with an input aperture of $f/18$. The mirror distance used in the interferometer was 2 mm. The entry and exit pinholes were 700 and 1000 μm in diameter, respectively, giving a tabulated machine finesse value of $F = 80$. A total of 2×10^4 measurement cycles were performed.

2.4. Micromagnetic Simulations

Micromagnetic simulations were conducted using the structural parameters given in **Table 2**, with the finite difference method software MicroMagnum.[36] We applied periodic boundary conditions for all field contributions in all spatial dimensions to simulate an infinitely extended material.[37] Rephrased from Torres et al., "the use of periodic boundary conditions implies that this one [unit cell] simulation represents an infinite array of [unit cells]."[38]

For each run, $H_0 = M_s = 5 \times 10^5 \, \text{Am}^{-1}$ was applied permanently, and the system relaxed to an initial state, after which it was left to oscillate freely for 50 ns. From the averaged directional magnetizations, the temporal magnetizations in the respective probing directions $\mathbf{k}$ were obtained, and the power spectra of their Fourier transforms were calculated. They were smoothed by a first-order Savitzky–Golay algorithm over ranges of 25 MHz to match the frequency resolution of the BLS spectra recorded from fabricated materials and normalized for presentation.

Table 2. Structural parameters of the characterized reference sample and the FCC inverse nickel opals: t thickness or $2r$ spherical void diameter, a side length of the FCC unit cell, f volumetric filling factor of the nickel phase.

| $t, 2r$ [nm]	a [nm]	$f/1$
Ref.: 300	–	–
245 ± 8	385 ± 13	0.46 ± 0.01
380 ± 12	625 ± 20	0.53 ± 0.01
410 ± 5	685 ± 10	0.55 ± 0.01
496 ± 8	816 ± 14	0.53 ± 0.01

2.5. Spin Wave Terminology and Frequency Boundaries

Magnon frequencies depend on the strengths of $\mathbf{H}_0$, the M_s of the material comprising the body, and whether the spins are coupled by exchange- or the longer-ranged dipole–dipole interaction. Depending on their propagation direction with regard to $\mathbf{H}_0$ and to the surfaces of the body, one distinguishes between bulk and surface spin waves. Combining the interaction types with the propagation directions leads to the three main types of modes.

The first type are dipole-coupled volume spin waves. If propagating in quasi-infinite volumes, they are simply termed "bulk magnons," as first described by Kittel.[39] In thin films, they are termed magnetostatic forward volume modes (MFVMs), or magnetostatic backward volume modes (MBVMs), for magnetization perpendicular to the film plane, or propagation and magnetization directions collinear in the film plane, respectively.[1]

The second type are dipole-coupled magnetostatic surface modes (MSMs) propagating parallel to surfaces, as formulated by Damon and Eshbach.[5] If the surface of the body is noncontinuous, these modes split discretely, as exemplified by a study of permalloy wires with varying separating distances.[11]

The third are exchange interaction-coupled spin waves propagating perpendicular between surfaces, the perpendicular standing modes (PSMs).[1] Being standing waves between confining surfaces of distance d, these modes are characterized by their order p, depending on the number of static nodes occurring along their length. Both MSM and PSM run perpendicular to magnetic field directions.[1]

To identify the nature of observed modes, their expected frequency ranges were determined. All calculations were performed in SI units, using the experimental parameters: The laser wavelength $\lambda = 532 \, \text{nm}$, the vacuum permeability $\mu_0 = 4\pi \times 10^{-7} \, \text{NA}^{-2}$, and exchange stiffness constant of nickel $A = 8 \, \text{pN}$[40] to calculate D, the exchange constant for the material, as well as the exact value for the electron gyromagnetic ratio γ'. From these parameters, the characteristic frequencies ν were calculated via Equation (2)–(8), and shown in **Figure 2**.[5,39,41]
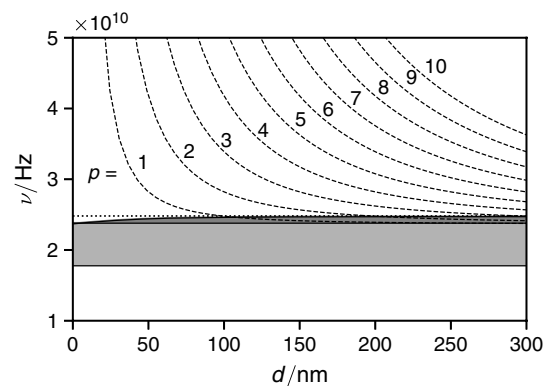
Figure 2. Plots of the expected spin wave frequency ranges for nickel, at $H_0 = 5 \times 10^5 \, \text{Am}^{-1}$. Solid lines mark the frequency boundaries $\Delta\nu_0$, $\Delta\nu_{HK}$, and $\Delta\nu_{DE}$ in order of ascending ν. Dotted lines: ν_{DE} as calculated by Equation (6), omitting the thickness dispersion.[1] Dashed lines: ν_P for $p = [1...10]$.

ADVANCED
SCIENCE NEWS
www.advancedsciencenews.com

physica pssb
status solidi
www.pss-b.com

$$D = \frac{2A}{\mu_0 M_s} \tag{2}$$

$$H_{ex} = D k^2 \tag{3}$$

$$\nu_0 = \gamma'(H_0 + H_{ex}) \tag{4}$$

$$\nu_{HK} = \gamma'[(H_0 + H_{ex})(H_0 + H_{ex} + M_s)]^{1/2} \tag{5}$$

$$\nu_{DE} = \gamma'(H_0 + H_{ex} + M_s/2) \tag{6}$$

$$H_p(d) = D\left(\frac{p\pi}{d}\right)^2 \tag{7}$$

$$\nu_p(d) = \gamma'[(H_0 + H_p(d))(H_0 + H_p(d) + M_s)]^{1/2} \tag{8}$$

Dipole-coupled volume waves (bulk, MFVM, and MBVM) are expected between ν_0 and ν_{HK}, the Herring–Kittel limit (equaling $\gamma\sqrt{BH}$ in Gaussian units).[5,31,42] MSMs are expected between ν_{HK} and ν_{DE}, the Damon–Eshbach limit.[5] In Figure 2, this global limit is presented together with the full dispersion relation for a compact thin film.[1]

For the material parameters used in micromagnetic simulations, and $\mathbf{k} = 0$, the following values, rounded to three significant figures, were obtained: $\nu_0 = 17.6$, $\nu_{HK} = 24.9$, and $\nu_{DE} = 26.4$ GHz. In BLS, spin wave frequencies are captured as laser frequency shifts $\Delta\nu$. For the fabricated and measured materials, probed with $k = k_i$, they were calculated as: $\Delta\nu_0 = 17.8$, $\Delta\nu_{HK} = 23.8$, and $\Delta\nu_{DE} = 24.8$ GHz.

The PSM do not have a fixed upper limit. Instead, they approach ν_{HK} with increasing d, and ∞ for $d \to 0$.[41] Figure 2 shows that their frequencies, for a given material and applied field, depend on p. Literature reports indicate that, typically, PSM intensities decay as $\propto p^{-1/2}$, due to eddy current magnetic damping.[43,44] Therefore, and based on the number of typically considered modes, we plotted $\nu_{p=10}$ as the upper boundary for observable PSM, in Figure 2 and in the presented results.

3. Results and Discussion

3.1. Nickel-Based 3D Antisphere Lattices

3D magnetic antisphere lattices based on nickel inverse opals were fabricated by a combination of colloidal sphere self-assembly and electrochemical infiltration.[24,27,34,35] By varying the diameters of the polystyrene templating spheres, FCC nickel inverse opals with different lattice constants a were obtained. Scanning electron micrographs of the different samples, recorded along the (1|1|1) direction of the FCC lattices, are shown in **Figure 3**.

All samples display a high degree of order and uniformity. However, due to the nature of the fabrication process, point, line, and edge defects typical of colloidal self-assembly templating and electrodeposition are present in all samples. Detailed structural analysis revealed lattice constants of 385, 625, 685, and 816 nm for the different samples. Key structural parameters are summarized in Table 2, and samples will be referred to by their respective values of a throughout this article.

To investigate the spin wave properties of the nickel inverse opals, we conducted BLS measurements, which were previously used to evaluate spin wave mode properties in 1D and 2D
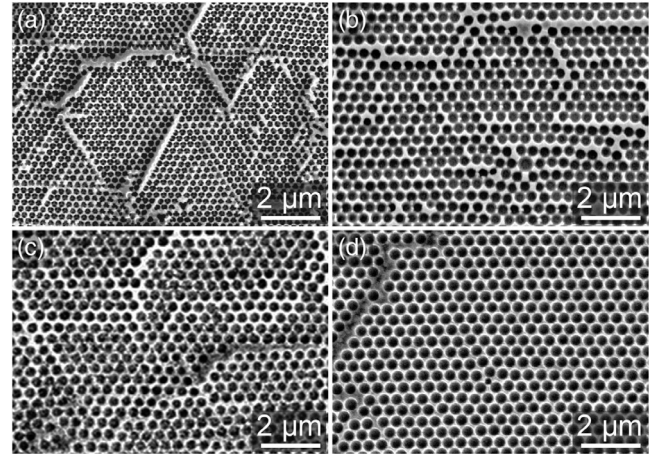

Figure 3. Scanning electron micrographs of the (1|1|1) surface planes of the fabricated nickel inverse opals with a of 385, 625, 685, and 816 nm (a–d, respectively).

magnonic crystals.[11,12,45] Recorded intensities due to inelastic scattering were identified by changing the strength of the field H_0 in steps to 0.0, 0.6×10^5, 1.7×10^5, and 5.0×10^5 Am^{-1}. When measuring with increasing H_0 (not shown for brevity), the recorded intensity maxima expectedly moved to larger frequencies, confirming their magnetic spin wave origin. The shifts of the PSM from the reference sample were used to estimate the materials' saturation magnetizations as $(4 \pm 1) \times 10^5$ Am^{-1}.

Figure 4 shows the BLS spectra measured at constant H_0 for the references sample and a nickel inverse opal sample, and for rotations around $\mathbf{H}_i$ and $\mathbf{E}_i$ (as defined in Table 1). All spectra were obtained from inelastic scattering, and thus were composed of asymmetrical Stokes and anti-Stokes shifts.

The reference sample is shown in Figure 4a. For the spectrum recorded in the $\mathbf{k} = (1|1|1)$ measurement orientation, a broad signal is located above $\Delta\nu_{DE}$, in the PSM frequency region. No modes are observed in the MSM frequency region between $\Delta\nu_{HK}$ and $\Delta\nu_{DE}$ (23.8–24.8 GHz) for $k = (1|1|1)$. The reason is that the component of $\mathbf{k}_i$ parallel to the sample surface, $\mathbf{k}_{i\|surf}$, is 0 in this orientation. However, we assigned as MSM two peaks, one visible in each of the Stokes-shifted parts of the spectra obtained from $\mathbf{k} = (5|5|2)$ and $(17|17|\bar{2})$ orientations (marked ↓). As expected, this mode shifts to higher $|\Delta\nu|$ for increased sample rotation around the $\mathbf{H}_0$ direction, which increases $\mathbf{k}_{i\|surf}$. The intensities recorded within the regions from $\Delta\nu_0$ to $\Delta\nu_{HK}$ are attributed to noise, in agreement with the expectation that no MBVMs are detectable with our measurement geometry.

BLS spectra of the nickel inverse opal sample with lattice constant 385 nm are shown in Figure 4b; those from 625, 685, and 816 nm are given in Figure S1a–c, Supporting Information. Spectra obtained for rotations around $\mathbf{H}_0$ (i.e., for $H_0 = (1|\bar{1}|0)$ and $\mathbf{k} = (1|1|1)$, $(5|5|2)$, $(17|17|\bar{2})$ and $(3|3|\bar{2})$, the gray plane in Figure 1a), are similar to one another, whereas those for rotations around $\mathbf{E}_i$ differ more strongly. Hence, the detected PSM are governed by the direction of $\mathbf{H}_0$. This can be rationalized by the comparatively isotropic strut geometries of the nickel inverse opals, in which PSM can run equally isotropically,[2] only being confined—true to their name—to planes perpendicular to $\mathbf{H}_0$.
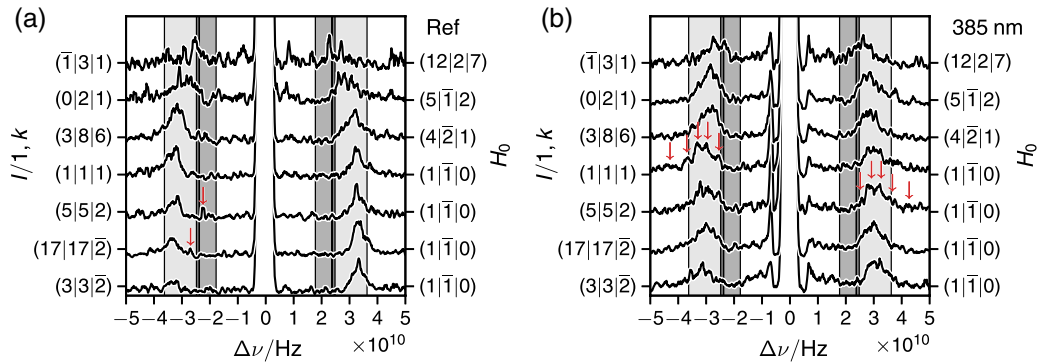
Figure 4. BLS spectra recorded at $H_0 = 5 \times 10^5$ Am^{-1} from a) the 300 nm thick reference, and b) the inverse opal with a of 385 nm for different $k \perp H_0$. Solid vertical lines mark the frequency boundaries $\Delta\nu_0$, $\Delta\nu_{HK}$, $\Delta\nu_{DE}$, and $\Delta\nu_{p=10}$ in order of ascending $|\Delta\nu|$. Arrows $\downarrow$ in (a) denote MSMs and in (b) PSMs.

In the $\mathbf{H}_0 = (1|\bar{1}|0)$ spectrum of the sample with the smallest lattice constant (385 nm), features between $\Delta\nu_{DE}$ and $\Delta\nu_{p=10}$ can be distinguished, as shown $\downarrow$ in Figure 4b. In Section 3.2, we will show that more PSM peaks can be expected from the samples with larger a. Unfortunately, in the spectra obtained from the three samples with larger lattice constants 625, 685, and 816 nm, the spectral resolution and signal-to-noise ratio are not sufficient to identify distinct modes.

The fine structures of the ferromagnetic resonance spectra reported by Kostylev et al., also for nickel inverse opals, are of similar complexity as the spectra reported in this article.[30] They stated that "[t]he presence of the fine structure in the out-of-plane data suggests that the broad absorption peaks seen in the in-plane FMR data in Figure 3 are absorption zones consisting of a number of weakly resolved resonances rather than a single resonance mode."[30] Kostylev et al. further assessed the effective exchange field ($H_{ex} = Dk^2$) for their observed modes, and noted that the resultant half-wavelengths (π/k) "are considerably smaller than the film thickness ($\approx$4.76 μm) but of the same order of magnitude as the mean width (90 nm) of basic elements [...]".[30]

The inverse opals assessed in this work have essentially the same parameters as Kostylev et al.'s: made from nickel by electrodeposition, with thicknesses on the micrometer scale, and with smallest strut diameters of $[54, 124, 148, 162]$ nm for $a = [385, 625, 685, 816]$ nm. Their further conclusion forms the basis for our model, proposed in Section 3.2: "Thus, in the framework of this model, the exchange contribution to the total energy of the standing spin wave originates from the nonuniformity of the Bloch-wave profile across the individual basic elements, but it is not given by the wave number of the standing Bloch wave $n\pi/L$, where $n = 0, 1, 2...$ (recall that $L = 4.76$ μm is the film thickness)."[30]

Our aforementioned observations highlight the limitation of BLS measurements, where signal strengths depend highly on ambient parameters such as variations in temperature, mechanical vibration, light scattering while passing through air, or electronic noise. Even in 1D and 2D magnonic crystals with near perfect, defect-free structures, BLS signals are, arguably, weak.[2,11,46–48] In 3D structures obtained by self-assembly, and with natural presences of point, line, and edge defects, the signal-to-noise ratios are further reduced; narrowly spaced modes are no longer distinguishable. Therefore, to interpret

BLS spectra for 3D samples, guidance is needed from simulations or numerically derived methods to determine correlations between 3D structure and resulting spin wave modes. This can be achieved by micromagnetic simulations. However, they require extensive computational resources and time. Therefore, we developed a simple numerical method to predict the PSM in 3D magnetic structures.

3.2. Tracing PSM by Pair Correlation Functions

Our approach to predict PSM in complexly porous materials—at the example of our antisphere lattices—was to calculate and convolve PSM, calculated from descriptors of the individual basic elements. These basic elements, the nickel struts interconnected throughout the material, are the proposed origin of complex spectra in the PSM regime.[30] As the basis for the descriptors, we calculated pair correlation functions $g(r)$ for all vectors normal to $\mathbf{H}_0$ that connect points equidistributed throughout the nickel phase. A number of points across a unit cell of $n = 35$ was determined as suitable. The solid phase pair distances r_s, normal to $\mathbf{H}_0$, provide an initial description of the characteristic distances along which PSM can propagate. They were histogrammed into $\sqrt{2}n$ bins over an array of distances r extending to the borders of a unit cell and used to calculate the pair correlation function, Equation (9).

$$g(r) = \frac{1}{4\pi r^2} \int \delta(r - r_s) \mathrm{d}r_s \qquad (9)$$

Hence, $g(r)$ is a measure of the probability of finding a distance $r_s \perp \mathbf{H}_0$. However, PSM in thin films are confined by the film thickness, i.e., between the surfaces. By analogy, the opal strut dimensions are proposed as the confining lengths. Therefore, we determined the edges of $g(r)$ as the maxima of its second-order derivative $g''(r)$, corresponding to the gradient change when passing a boundary between solid material and air. The results were $\hat{g}(r)$, the values of $g(r)$ at the maxima of $g''(r)$.

For each $\mathbf{H}_0$, the scalar d in Equation (7) and (8) was then substituted with arrays of r, resulting in arrays of frequencies $\nu_p(r)$ for each mode number p, to which belong arrays of magnitudes $\hat{g}(r)$. The expected convolved PSM spectrum was then calculated by Equation (10).

$$I(\nu) = \sum_{p=1}^{10} \hat{g}(\nu_p(r))p^{-1/2} \tag{10}$$

In detail, we binned the $\hat{g}(\nu_{\rm p}(r))$ into equal-width values of ν, spanning the range of $\nu_{\rm p}(r)$. The factor $p^{-1/2}$ accounts for magnetic damping. To verify and refine our approach, we first calculated the expected convolved PSM spectrum for our reference sample by Equation (10). Calculating $\nu_{\rm p}$ via Equation (8) does not provide a distribution of $I(\nu)$.[44] Using $d = 300\,{\rm nm}$, divided by the cosine of the angle of rotation around $\mathbf{E}_{\rm i}$, and comparing preliminary results to the measured spectra (Figure 4a) allowed us to tune the peak shape via the use of a Gaussian signal window, **Figure 5**a. We applied the same shaping approach during the calculation of $I(\nu)$ for the inverse opal slices, yielding the predicted spectra shown in Figure 5b–e.

The following similarities between the predicted and the recorded patterns from Figure 4 and 5a,b can be discerned: 1) The convolution of $I(\nu)$ into broadened signals within the PSM range; 2) The respective number of maxima within the PSM range; 3) For inverse opals, the loss of fine structure with $\mathbf{H}_0 \rightarrow (4|\bar{2}|1) \rightarrow (5|\bar{1}|2) \rightarrow (12|2|7)$; 4) For the reference sample, the shift of large $I(\nu)$ to lower frequencies with $\mathbf{H}_0 \rightarrow (4|\bar{2}|1) \rightarrow (5|\bar{1}|2) \rightarrow (12|2|7)$

As pointed out earlier, we considered the recorded BLS spectra an insufficient basis for comparison. Hence, in the following sections, we discuss our predictions together with simulated spectra.

### 3.3. Interpretation and Micromagnetic Simulations

Micromagnetic simulations of nickel inverse opals were conducted for a wide spectral range. **Figure 6** shows the entire set of simulated spectra for nickel inverse opals samples with $M_{\rm s} = 5 \times 10^5\,{\rm Am}^{-1}$, different lattice constants, and for rotations around $\mathbf{H}_0$ and $\mathbf{E}_{\rm i}$ as defined in Table 1. Common to all spectra are distinct features in the PSM region, between $\nu_{\rm DE} = 26.4\,{\rm GHz}$ and $\approx 45\,{\rm GHz}$. These remain virtually unchanged for rotations around $\mathbf{H}_0$ (i.e., for $\mathbf{H}_0 = (1|\bar{1}|0)$ and $\mathbf{k} = (1|1|1)$, $(5|5|2)$, $(17|17|\bar{2})$, and $(3|3|\bar{2})$), probing the plane indicated gray in Figure 1a. We interpret this as further confirmation that they are indeed PSM, confined between basic structural elements within the plane normal to $\mathbf{H}_0 = (1|\bar{1}|0)$.

The same features (1)–(3), outlined in Section 3.2, are observable in the simulated spectra. However, (2) requires some qualification: while our manner of tracing PSM is straightforward, it depends on either analytically determining directional $g(r)$ (laborious), or the use of numerical structure descriptions (our choice). To achieve computation times on the order of minutes with a current desktop computer, signal levels and frequency resolutions are balanced by the data bin sizes, effectively limiting the latter.

Another notable point is that we calculated the spectra in Figure 5 according to the simulation parameters. Therefore, the number and position of PSMs observable in Figure 6 is the same, whereas in Figure 4, their positions are shifted to lower $|\Delta\nu|$.

Our general interpretation of the correlation between unit cell size a and PSM maxima is as follows: due to the nearly constant filling factor f (see Table 2), the strut diameters increase with a. This necessitates a shift of maxima of $g''(r)$ to larger r, which in turn means a reduction of $H_p(r)$ with increasing a, Equation (8). In the inverse opals, the maxima of $g''(r)$ occur at lengths smaller than $d = 300\,{\rm nm}$, leading to PSM frequencies larger than those observed in the reference sample. The first two strongest maxima
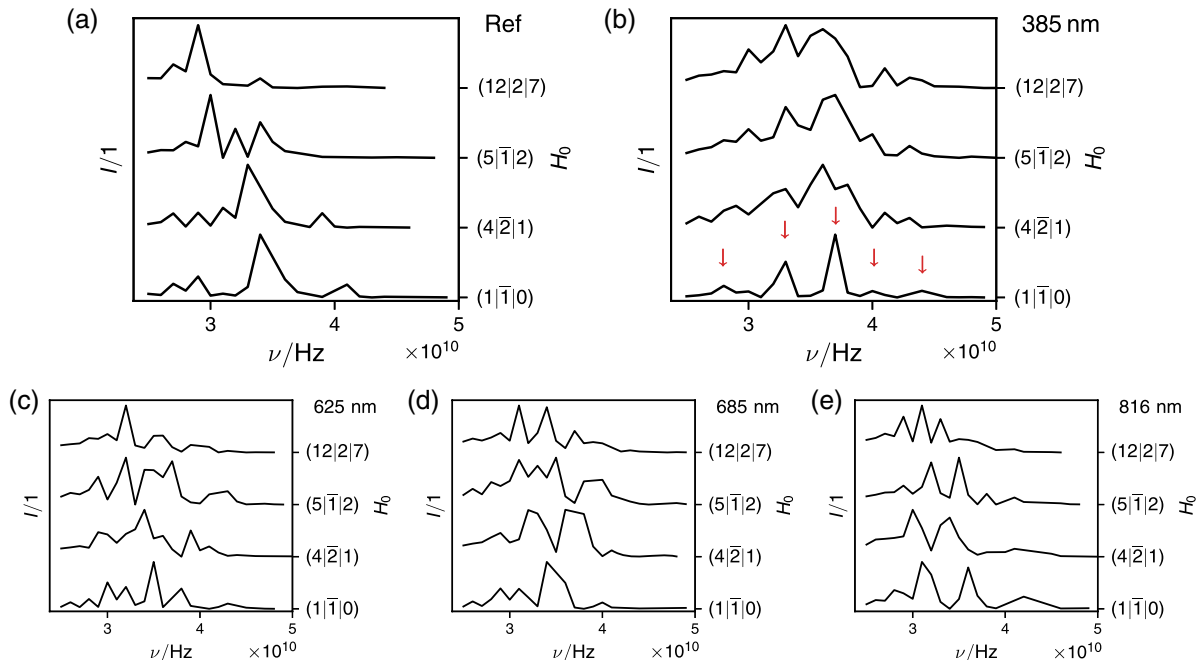
Figure 5. Predicted spectra for different $\mathbf{H}_0$ at $H_0 = 5 \times 10^5\,{\rm Am}^{-1}$ in the PSM frequency range obtained by applying $\hat{g}(\nu_p(r))$ from simulation models to Equation (8)–(10), for a 300 nm-thick nickel film (a), and nickel FCC antisphere lattices with a of 385, 625, 685, and 816 nm (b–e, respectively). Arrows ↓ denote predicted PSMs, for the continuing example of $a = 385$ nm.
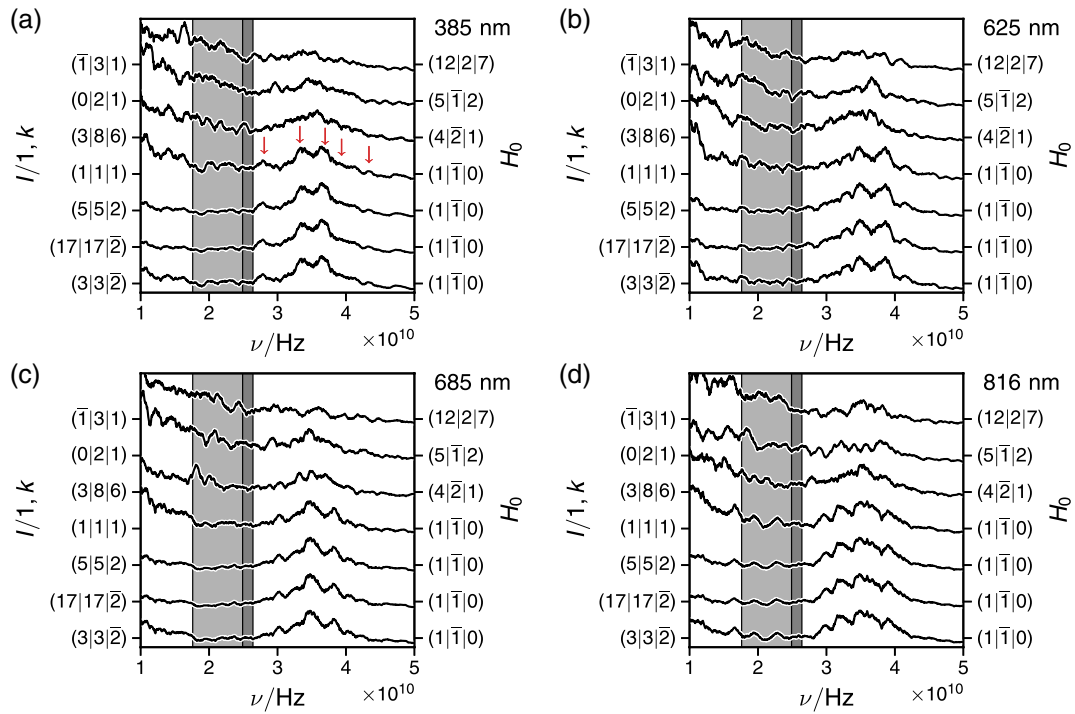
Figure 6. Frequency transform spectra obtained by dynamically simulating nickel inverse opals with a of 385, 625, 685, and 816 nm (a–d, respectively) at $H_0 = 5 \times 10^5$ Am^{-1} and for different $\mathbf{k} \perp \mathbf{H}_0$. Solid vertical lines mark the frequency boundaries $\Delta\nu_0$, $\Delta\nu_{HK}$, and $\Delta\nu_{DE}$ in order of ascending ν. Arrows ↓ denote observed PSMs for the exemplary $a = 385$ nm.
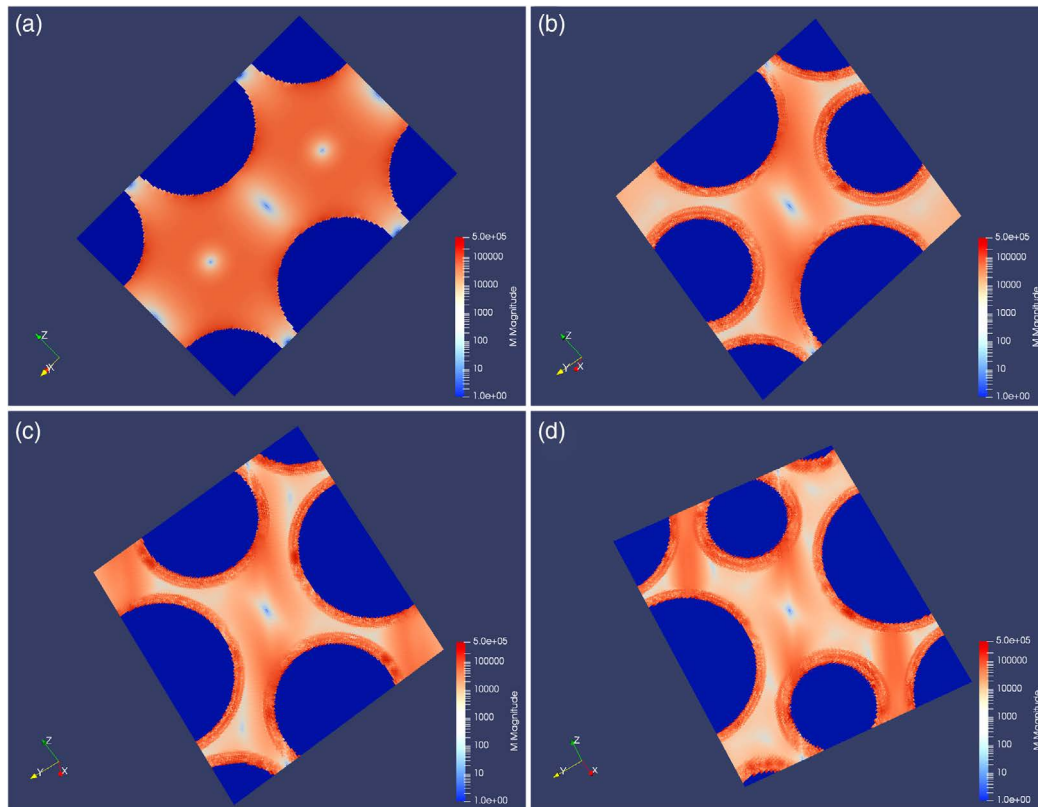
Figure 7. Directional slice views of $\mathbf{H}_{ex}$ at the beginning of simulations, through the center of an $a = 816$ nm unit cell (qualitatively representative of all unit cell sizes), normal to a) $(1|\bar{1}|0)$, b) $(4|\bar{2}|1)$, c) $(5|\bar{1}|2)$, and d) $(12|2|7)$.

of $g''(r)$ for $\mathbf{H}_0 = (1|\bar{1}|0)$ were at $a \cdot [0.17, 0.29]$. For example, in the smallest tested unit cell, $385\,\text{nm} \cdot [0.17, 0.29] = [65\,\text{nm}, 112\,\text{nm}]$. Hence, the maxima positions approximate, within the binning resolution, the calculated smallest diameters of the basic elements in lattice directions $\langle 1|1|0 \rangle$ of 54 nm, and $\langle 1|0|0 \rangle$ of 2×54 nm, respectively.

To correlate our results to observable features of $\mathbf{H}_{ex}$, we extracted slices normal to the directions of the applied external field $\mathbf{H}_0$, **Figure 7**. While the images only depict single slices instead of all vectors $\perp \mathbf{H}_0$, they reveal features that intuitively account for the observed mode spectra: perpendicular to $(1|\bar{1}|0)$, Figure 7a, $\mathbf{H}_{ex}$ appears smooth and circularly symmetric around minima of $\mathbf{H}_{ex}$, and the minimum strut diameter in direction $\langle 1|1|0 \rangle$ can be discerned. Our interpretation is that this high degree of symmetry leads to the comparatively low number of distinct PSM maxima observable in Figure 5b and 6a. For all other directions (Figure 7b–d), the magnitude of $\mathbf{H}_{ex}$ appears only twofold point-symmetric around its minima. Here, the expectation—by analogy to diffraction processes in atomic crystals—that reduced symmetries lead to larger numbers of observable signals, is confirmed by the observations from Figure 5 and 6.

4. Conclusions

We have introduced a numerical method to predict how spin wave spectra of nickel are altered in the presence of a 3D super-lattice such as an inverse opal. Both the mode splitting and positions were derived and interpreted by applying selected pair correlations to the perpendicular standing wave exchange factor. The method enables fast and simple assessment of spin wave modes in 3D magnetic superstructures without the need of expensive and time-consuming simulations. In reverse, our numerical method may be adapted to interpret convoluted BLS spectra. This was shown to be particularly challenging for complex 3D magnetic structures obtained by self-assembly methods. These materials not only contain structural defects (point, line, and edge defects in the superlattice) but also possess strongly scattering surfaces. While BLS has provided high-quality experimental data on magnetic spin waves in planar systems, we found its application to highly scattering surfaces of complex 3D structures of limited usefulness. We further anticipate the presented method based on pair correlation functions, which can rapidly predict splitting and spacing of spin wave modes, to be an aid for the tailored design of materials with complex or disordered geometries, for which so far ab initio calculations have been used.[28,49,50]

Supporting Information

Supporting Information is available from the Wiley Online Library or from the author.

Conflict of Interest

The authors declare no conflict of interest.

[1] S. O. Demokritov, B. Hillebrands, A. N. Slavin, *Phys. Rep.* **2001**, *348*, 441.

[2] S. Tacchi, G. Gubbiotti, M. Madami, G. Carlotti, *J. Phys.: Condens. Matter* **2016**, *29*, 073001.

[3] M. Krawczyk, H. Puszkarski, *Phys. Rev. B* **2008**, *77*, 054437.

[4] R. W. Damon, J. Eshbach, *J. Phys. Chem. Solids* **1961**, *19*, 308.

[5] J. Eshbach, R. Damon, *Phys. Rev.* **1960**, *118*, 1208.

[6] A. Chumak, P. Pirro, A. Serga, M. Kostylev, R. Stamps, H. Schultheiss, K. Vogt, S. Hermsdoerfer, B. Laegel, P. Beck, B. Hillebrands, *Appl. Phys. Lett.* **2009**, *95*, 262508.

[7] A. Chumak, A. Serga, S. Wolff, B. Hillebrands, M. Kostylev, *Appl. Phys. Lett.* **2009**, *94*, 172511.

[8] S. Neusser, D. Grundler, *Adv. Mater.* **2009**, *21*, 2927.

[9] P. Gruszecki, M. Krawczyk, *Wiley Encyclopedia of Electrical and Electronics Engineering*, John Wiley & Sons, Inc., Hoboken, NJ **1999**, pp. 1–23.

[10] S. Nikitov, P. Tailhades, C. Tsai, *J. Magn. Magn. Mater.* **2001**, *236*, 320.

[11] J. Jorzick, S. Demokritov, C. Mathieu, B. Hillebrands, B. Bartenlian, C. Chappert, F. Rousseaux, A. Slavin, *Phys. Rev. B* **1999**, *60*, 15194.

[12] M. Kostylev, A. Stashkevich, N. Sergeeva, *Phys. Rev. B* **2004**, *69*, 064408.

[13] V. Zhang, H. Lim, C. Lin, Z. Wang, S. Ng, M. Kuok, S. Jain, A. Adeyeye, M. Cottam, *Appl. Phys. Lett.* **2011**, *99*, 143118.

[14] M. Kostylev, S. Zhong, J. Ding, A. O. Adeyeye, *J. Appl. Phys.* **2013**, *114*, 113910.

[15] L. Giovannini, F. Montoncello, F. Nizzoli, *Phys. Rev. B* **2007**, *75*, 024416.

[16] S. Tacchi, F. Montoncello, M. Madami, G. Gubbiotti, G. Carlotti, L. Giovannini, R. Zivieri, F. Nizzoli, S. Jain, A. Adeyeye, N. Singh, *Phys. Rev. Lett.* **2011**, *107*, 127204.

[17] H. Ulrichs, B. Lenk, M. Münzenberg, *Appl. Phys. Lett.* **2010**, *97*, 092506.

[18] G. Duerr, M. Madami, S. Neusser, S. Tacchi, G. Gubbiotti, G. Carlotti, D. Grundler, *Appl. Phys. Lett.* **2011**, *99*, 202502.

[19] J. Vasseur, L. Dobrzynski, B. Djafari-Rouhani, H. Puszkarski, *Phys. Rev. B* **1996**, *54*, 1043.

[20] S. Tacchi, G. Duerr, J. Klos, M. Madami, S. Neusser, G. Gubbiotti, G. Carlotti, M. Krawczyk, D. Grundler, *Phys. Rev. Lett.* **2012**, *109*, 137202.

[21] M. Krawczyk, S. Mamica, M. Mruczkiewicz, J. Klos, S. Tacchi, M. Madami, G. Gubbiotti, G. Duerr, D. Grundler, *J. Phys. D: Appl. Phys.* **2013**, *46*, 495003.

[22] S. Mamica, M. Krawczyk, D. Grundler, *Phys. Rev. Appl.* **2019**, *11*, 054011.

[23] E. Beginin, A. Sadovnikov, A. Y. Sharaevskaya, A. Stognij, S. Nikitov, *Appl. Phys. Lett.* **2018**, *112*, 122404.

[24] P. N. Bartlett, M. A. Ghanem, I. S. El Hallag, P. de Groot, A. Zhukov, *J. Mater. Chem.* **2003**, *13*, 2596.

[25] Y. Hao, F. Zhu, C. Chien, P. C. Searson, *J. Electrochem. Soc.* **2007**, *154*, D65.

[26] M. Okuda, T. Schwarze, J. Eloi, S. W. Jones, P. Heard, A. Sarua, E. Ahmad, V. Kruglyak, D. Grundler, W. Schwarzacher, *Nanotechnology* **2017**, *28*, 155301.

[27] G. Hukic-Markosian, Y. Zhai, D. E. Montanari, S. Ott, A. Braun, D. Sun, Z. V. Vardeny, M. H. Bartl, *J. Appl. Phys.* **2014**, *116*, 013906.

[28] D. Volkov, A. Zheltukhin, *Zh. Eksp. Teor. Fiz.* **1980**, *78*, 1867.

[29] S. Mamica, M. Krawczyk, M. Sokolovskyy, J. Romero-Vivas, *Phys. Rev. B* **2012**, *86*, 144402.

[30] M. Kostylev, A. Stashkevich, Y. Roussigné, N. Grigoryeva, A. Mistonov, D. Menzel, N. Sapoletova, K. Napolskii, A. Eliseev, A. Lukashin, S. V. Grigoriev, *Phys. Rev. B* **2012**, *86*, 184431.

[31] L. Walker, *Phys. Rev.* **1957**, *105*, 390.

[32] P. Fletcher, R. Bell, *J. Appl. Phys.* **1959**, *30*, 687.

[33] C. Neugebauer, *Phys. Rev.* **1959**, *116*, 1441.

[34] X. Yu, Y.-J. Lee, R. Furstenberg, J. O. White, P. V. Braun, *Adv. Mater.* **2007**, *19*, 1689.

[35] H. Zhang, P. V. Braun, *Nano Lett.* **2012**, *12*, 2778.

[36] C. Abert, G. Selke, B. Kruger, A. Drews, *IEEE Trans. Magn.* **2011**, *48*, 1105.

[37] B. Krüger, G. Selke, A. Drews, D. Pfannkuche, *IEEE Trans. Magn.* **2013**, *49*, 4749.

[38] L. Torres, L. Lopez-Diaz, O. Alejos, *J. Appl. Phys.* **2000**, *87*, 5645.

[39] C. Kittel, *Phys. Rev.* **1947**, *71*, 270.

[40] P. Talagala, P. S. Fodor, D. Haddad, R. Naik, L. Wenger, P. Vaishnava, V. Naik, *Phys. Rev. B* **2002**, *66*, 144426.

[41] B. Lenk, G. Eilers, J. Hamrle, M. Münzenberg, *Phys. Rev. B* **2010**, *82*, 134443.

[42] C. Herring, C. Kittel, *Phys. Rev.* **1951**, *81*, 869.

[43] M. A. Schoen, J. M. Shaw, H. T. Nembach, M. Weiler, T. J. Silva, *Phys. Rev. B* **2015**, *92*, 184417.

[44] H. Qin, S. J. Hämäläinen, S. Van Dijken, *Sci. Rep.* **2018**, *8*, 5755.

[45] G. Gubbiotti, S. Tacchi, M. Madami, G. Carlotti, A. Adeyeye, M. Kostylev, *J. Phys. D: Appl. Phys.* **2010**, *43*, 264003.

[46] A. Stashkevich, Y. Roussigne, A. Stognij, N. Novitskii, M. Kostylev, G. Wurtz, A. Zayats, L. Lutsev, *Phys. Rev. B* **2008**, *78*, 212404.

[47] Z. Wang, M. Kuok, S. Ng, D. Lockwood, M. Cottam, K. Nielsch, R. Wehrspohn, U. Gösele, *Phys. Rev. Lett.* **2002**, *89*, 027201.

[48] G. Gubbiotti, G. Carlotti, T. Okuno, T. Shinjo, F. Nizzoli, R. Zivieri, *Phys. Rev. B* **2003**, *68*, 184409.

[49] D. Huber, *Phys. Rev. B* **1973**, *8*, 2124.

[50] S. K. Das, V. N. Singh, P. Majumdar, *Phys. Rev. B* **2013**, *88*, 214428.